MEASUREMENT OF ANGULAR COEFFICIENTS OF DRELL-YAN e^+e^- PAIRS IN $p\bar{p}$ COLLISIONS AT $\sqrt{s} = 1.96$ TeV

Sudeep Singh Bhatia

A dissertation submitted in partial fulfillment
of the requirements for the degree of

Masters of Science
in Physics
Department of Physics and Astronomy

University of Mississippi

2013

Copyright © 2013 by Sudeep Singh Bhatia

All rights reserved.

Abstract

In this thesis we present the status of the measurement of angular distributions of final state electrons in $p\bar{p} \rightarrow \gamma^*/Z \rightarrow e^+e^- + X$ events produced in the Z boson mass region at $\sqrt{s} = 1.96$ TeV at the Tevatron. For this analysis, we are using the full Run II dataset corresponding to $9.7 fb^{-1}$ of integrated luminosity collected with the DØ detector. The angular distributions as a function of the transverse momentum of the electron-positron pair are studied, and the Lam-Tung relation, valid only for a spin-1 description of the gluon is investigated. The final result will also describe the details of the production mechanism of Z bosons via quark anti-quark annihilation or quark-gluon Compton scattering.

Dedicated To

My Parents.

Acknowledgments

I would like to express my deepest appreciation to my advisor Dr. Breese Quinn and my committee members, Dr. Donald Summers, Dr. Joseph R. Gladden, and Dr. Nathan Hammer. I could not have financed my studies without the assistant-ship provided by the Department of Physics and Astronomy.

In addition, I express my sincere thanks to Dr. Hang Yin, of Fermilab, who provided invaluable help all along from the beginning. Without his direction, steadiness and practicality, I would have never completed this thesis that required me to learn so many things at once.

Table of Contents

Abstract ii

Dedicated To iii

Acknowledgments iv

List of Figures vii

List of Tables ix

1 Introduction 1

1.1 Standard Model 1

1.2 A Few Definitions 2

1.3 Introduction: Drell-Yan Theory 5

2 Experimental Apparatus 10

2.1 The Tevatron Accelerator 10

2.2 The DØ detector 12

2.2.1 Central Tracking System 13

2.2.2 Calorimeter 14

2.2.3 Muon System 16

2.2.4 Trigger System 17

3 Analysis technique **18**

3.1 Event Selection 18

3.2 Simulation 20

3.3 Efficiency Studies 20

3.4 Charge Mis-identification 27

3.5 Background Estimation 28

3.6 PYTHIA vs ALPGEN + PYTHIA for $W + X$ 30

3.7 Extraction of Coefficients 30

3.8 Future Work 32

3.8.1 Energy Scale and Resolution 32

3.9 Systematic Uncertainities 34

4 Summary **36**

Bibliography **38**

List of Figures

Figure Number Page

1.1 The elementary particles in the Standard Model. 2

1.2 Z-axis, psuedo-rapidity and transverse momentum in the DØ reference frame. . 4

1.3 Tree level Feynman diagram of the Drell-Yan process. 5

1.4 Leading order annihilation and Compton diagrams. 6

1.5 Collins-Soper Frame. 7

1.6 Forward-Backward Events. 9

2.1 Schematic diagram of the Fermilab's accelerator chain 12

2.2 A view of the DØ Run II upgraded detector. 13

2.3 Layout of the SMT. The barrels, F-disks and H-disks are labelled. 14

2.4 DØ tracking detector 15

2.5 DØ calorimeter detector 16

3.1 EM ID efficiency and scale factors vs electron p_T in CC region. 24

3.2 Tracking efficiency and scale factors vs electron p_T in CC region. 24

3.3 EM Id efficiency and scale factors vs electron p_T in EC region. 25

3.4 Tracking efficiency and scale factors vs electron p_T for type 2 electrons in EC region. 25

3.5 Tracking efficiency and scale factors vs electron p_T for type 3 electrons in EC region. 25

3.6 Tracking efficiency and scale factors vs electron p_T for type 4 electrons in EC region. 26

3.7 Charge mis-identification rate for electron p_T (Run IIb2) 28

3.8 Invariant mass (left), Z p_T (right) signal and background distributions. 29

3.9 The Collins-Soper $\cos\theta^*$ and ϕ^* distribution for W+X background 30

3.10 Comparison between ALPGEN + PYTHIA , and PYTHIA for W+X background . 31

3.11 Measured values of A_0 , A_2 , A_3, and A_4 coefficients. 33

List of Tables

Table Number Page

3.1 ALPGEN + PYTHIA vs PYTHIA : Z_{p_T} in 5 p_T bins for all regions. 30

3.2 ALPGEN + PYTHIA vs PYTHIA : Z_{p_T} in 5 p_T bins for CCCC regions. 31

3.3 ALPGEN + PYTHIA vs PYTHIA : Z_{p_T} in 5 p_T bins for CCEC regions. 31

3.4 ALPGEN + PYTHIA vs PYTHIA : Z_{p_T} in 5 p_T bins for ECEC regions. 32

Chapter 1

Introduction

1.1 Standard Model

The science of elementary particle physics attempts to discover the fundamental building blocks of the universe and to describe the laws of nature at the fundamental level. In order to probe the matter at hadronic scales ($\leq 10^{-15}$ m), one requires high energy ($\sim$ 1 GeV), in accordance with de Broglie relation ($\lambda = hc/E$). This is why elementary particle physics may also be called High Energy Physics. In 1960's Glashow [1], Weinberg [2], and Salam [3], in a series of papers, proposed the theory to describe the elementary interactions which is known as the Standard Model (SM) of particle physics. The SM has been extremely successful in describing the electro-magnetic, weak, and strong force. However, the most familiar gravitational force is left out and has been a theoretical challenge to include.

At a fundamental level, all particles are classified into two classes, bosons and fermions. Bosons are the force carriers between fermions and have integral spin. Spin-1 vector bosons, like the photon (γ) is a carrier of the electromagnetic force. The $W^{\pm}$ and Z bosons are mediators of the weak force which explains nuclear decays. The gluon (g) binds quarks inside the nucleus, and is the strong force quanta. Two or more bosons with identical properties can be in the same place at the same time.

On the other hand, fermions are matter particles with spin $\frac{1}{2}$. They obey Pauli's exclusion principle, according to which, two identical fermions cannot occupy same quantum state simultaneously. The are two types of fermions: leptons (l) and quarks (q). There are six

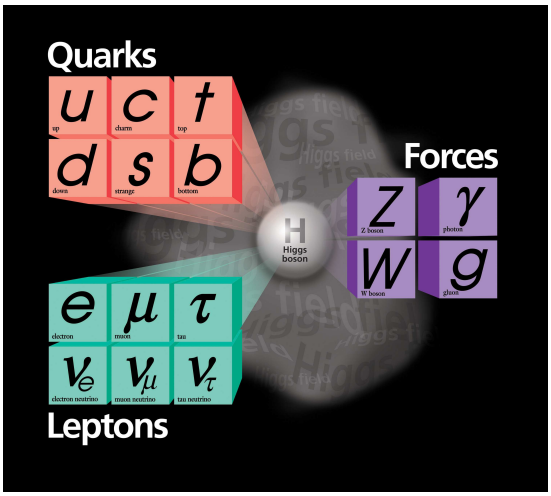

Figure 1.1. The elementary particles in the Standard Model.

flavors of leptons : the electron (e), the muon (μ), the tau (τ), and their corresponding neutrinos (ν_e, ν, ν_τ). The charged leptons interact via the electromagnetic and weak forces, while the neutrinos, which carry no charge, interact only via the weak force. There are also six flavors of quarks : up (u), down (d), charm (c) , strange (s), top (t) and bottom (b). Unlike the leptons, they possess fractional electric charges.

The SM also predicts a spin-0 scalar Higgs Field (H), which provides masses to weak bosons and fermions.

1.2 A Few Definitions

In 1969, Richard Feynman [4] proposed that nucleons (protons or neutrons) are not elementary, but a bound systems of quarks (q), anti-quarks ($\bar{q}$) and gluon (g), collectively called partons. Each parton carries a fraction, x of longitudinal momentum of the parent nucleon. The momentum distribution functions of the partons within the nucleon are called Parton Distribution Functions (PDFs). For example, the PDF $f_i(x, Q^2)$ gives the probability of finding a parton of flavour i (quarks or gluon) in a proton carrying a fraction x of the proton's momentum, with Q being the energy scale of the hard interaction.

In this thesis, we will investigate the production of electron-positron pairs by parton

annihilation in collisions of protons with anti-protons. The data for my thesis comes from the DØ detector located at the Fermi National Accelerator Laboratory, Batavia, IL. In the DØ detector frame of reference, the positive z axis is defined along the proton beam direction, the y axis is upward, and the x axis points to the centre of the accelerator. The azimuthal and polar angles are denoted as ϕ and θ, respectively. A vector pointing towards the centre of the accelerator defines $\phi = 0$, and ϕ increases anti-clockwise, such that $\phi = \pi/4$ points upwards.

Another commonly used variable for locating polar coordinates is the psuedo-rapidity, η. It is defined as $\eta = -ln[\tan(\theta/2)]$. The region of small $|\eta|$ ($|\eta| < 1$) is referred to as "central", and the region of larger $|\eta|$ as forward.

The rapidity is defined as

$$y = \frac{1}{2} ln \frac{E + p_z}{E - p_z},$$

where E is energy and p_z is the z-component of the momentum parallel to the beam. For a non-relativistic particle, rapidity is the same as the velocity along z-axis. In the relativistic limit $p >> m$, that is, the mass of the particle is small compared to its momentum (for example a relativistic electron), rapidity approximates psuedo-rapidity.

The relativistic invariant mass (M_{ll}) of a lepton pair (say electron-positron e^+e^-) is given by,

$$M_{ll} = \sqrt{(E_{l^+} + E_{l^-})^2 + (\boldsymbol{p}_{l^+} + \boldsymbol{p}_{l^-})^2},$$

where, E is energy and $\boldsymbol{p}$ is the vector momentum of a given lepton. The transverse component of energy and momentum is defined as $E_T = Esin\theta$ and $p_T = Psin\theta$, respectively.

The cross-section, σ, is a measure of the interaction probability per unit flux. In collider experiments, the flux corresponds to the size and amount of particles in the colliding beams and is referred to as luminosity, $\mathcal{L}$. The luminosity depends on a number of beam characteristics at the interaction point like the number of particles in each colliding beam, number

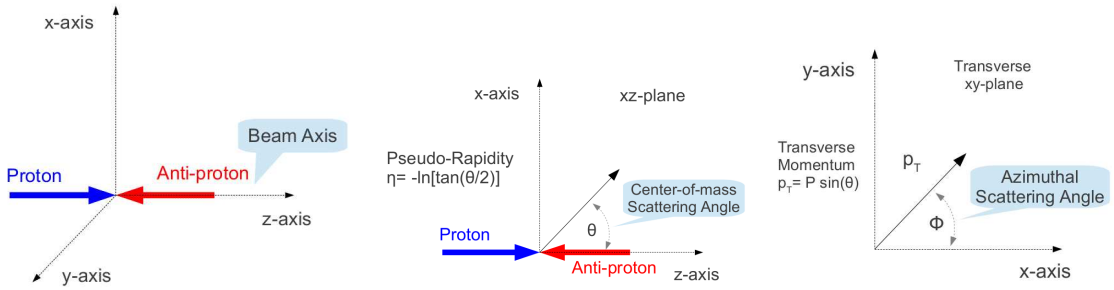

Figure 1.2. Z-axis, psuedo-rapidity and transverse momentum in the center-of-mass reference frame at DØ.

of bunches, and the transverse sizes of the bunches. The luminosity is given as:

$$\mathcal{L} = \frac{f_{rev} B N_p N_{\overline{p}}}{4\pi(\sigma_p^2 + \sigma_{\overline{p}}^2)} F(\sigma_l/\beta^*), \tag{1.1}$$

where f_{rev} is the revolution frequency, B is the number of bunches per beam, $N_{p(\overline{p})}$ is the number of protons (anti-protons) per bunch, $\sigma_{p(\overline{p})}$ is the transverse beam size of the proton (anti-proton) beam, and F is a form factor depending on the bunch length (σ_l) and the beta function at the interaction point (β^*). The Luminosity is thus proportional to the product of the number of particles in each beam passing through a unit area per unit time and is expressed in units of $\text{cm}^{-2}\text{s}^{-1}$. The cross-section is expressed in units of barns where 1 barn$\equiv 10^{-24}$ cm^2. An important quantity is the number of interactions (N) occurring in collisions over a given period of time. The number of times a given process occurs, N, is given by

$$N = \sigma \int \mathcal{L} dt \tag{1.2}$$

Where $\int \mathcal{L}$ dt is the luminosity integrated over time and it is referred to as the integrated luminosity, and is measured in units of inverse barns (b^{-1}). Typical cross-sections for various interesting physical processes are usually of the order of pico-barns (pb), or $\equiv 10^{-36}$ cm^2. Thus integrated luminosity is often measured in inverse pico-barns (pb^{-1}). For example, a certain process of 1 pb cross-section is expected to occur 100 times during the delivery of

100 pb^{-1} of integrated luminosity.

1.3 Introduction: Drell-Yan Theory

The production of oppositely charged lepton pairs ($e^-e^+, \mu^-\mu^+$, or $\tau^-\tau^+$) in hadron collisions by annihilation of a $q\bar{q}$ pair is called the Drell-Yan process [5]. For example, in proton-antiproton ($p\bar{p}$) collisions, a q from one hadron undergoes annihilation with an $\bar{q}$ from another hadron to create a Z boson or virtual photon (γ^*), which can decay to oppositely charged leptons as shown in Figure 1.3.

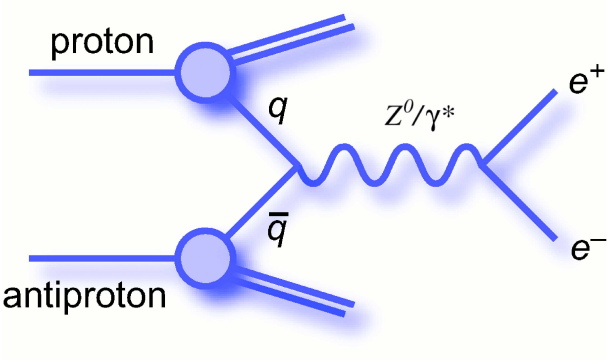

Figure 1.3. Tree level Feynman diagram of the Drell-Yan process.

According to vector-axial (V-A) theory [5], the decay angular distribution in the Z/γ^* rest frame is,

$$\frac{d\sigma}{d(\cos\theta)} \propto (1 + \cos^2\theta). \tag{1.3}$$

However, in general, the Z/γ^* is produced with a finite transverse momentum. According to Quantum Chromodynamics (QCD) at leading order (LO), this can occur either by emission of a gluon g or quark q in the final state via $q\bar{q}$ annihilation or qg Compton scattering (Figure 1.4).

The angular distribution of final state electrons in colliding hadron beams are best described in the rest frame of Z boson called the Collins-Soper (CS) frame. The general expression [6, 7] for the angular distribution of the final state electron in the Collins-Soper frame (Figure 1.5) is,

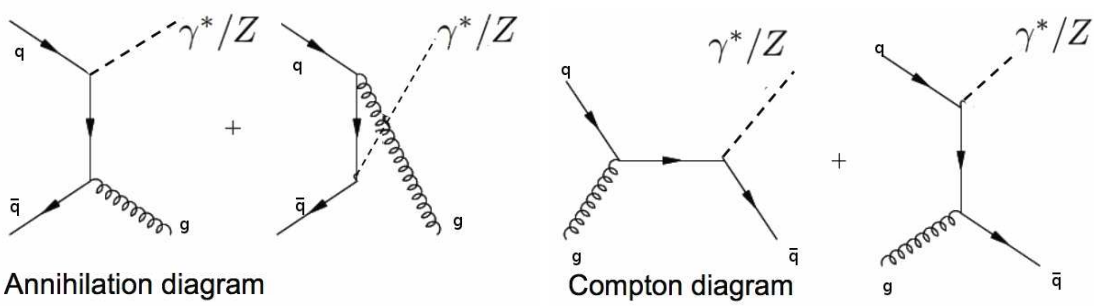

Figure 1.4. Leading order annihilation ($q\bar{q} \to Z/\gamma^* g$) and Compton ($qg \to Z/\gamma^* q$) diagrams for the production of Z bosons with finite transverse momentum.

$$\begin{aligned}
\frac{d\sigma}{d\cos\theta^* d\phi^*} &\propto (1+\cos^2\theta^*) \\
&+ \frac{1}{2}A_0(1-3\cos^2\theta^*) + A_1 \sin 2\theta^* \cos\phi^* \\
&+ \frac{1}{2}A_2 \sin^2\theta^* \cos 2\phi^* + A_3 \sin\theta^* \cos\phi^* \\
&+ A_4 \cos\theta^* + A_5 \sin^2\theta^* \sin 2\phi^* \\
&+ A_6 \sin 2\theta^* \sin\phi^* + A_7 \sin\theta^* \sin\phi^*.
\end{aligned} \tag{1.4}$$

When integrated over ϕ^*, (1.4) is given by,

$$\frac{d\sigma}{d\cos\theta^*} \propto (1+\cos^2\theta^*) + \frac{1}{2}A_0(1-3\cos^2\theta^*) + A_4\cos\theta^*, \tag{1.5}$$

and when integrated over $\cos\theta^*$, it is,

$$\frac{d\sigma}{d\phi^*} \propto 1 + \frac{3\pi}{16}A_3\cos\phi^* + \frac{1}{4}A_2\cos 2\phi^* + \frac{3\pi}{16}A_7\sin\phi^* + \frac{1}{4}A_5\sin 2\phi^*. \tag{1.6}$$

Here, θ^* and ϕ^* are the polar and azimuthal angles of the electron in the CS frame (Figure 1.5). The CS frame is the special rest frame of the Z boson. The z-axis is defined as the bisector of angle between the proton (p) beam momentum ($\boldsymbol{P}$) and the negative of the $\bar{p}$ beam momentum ($-\bar{\boldsymbol{P}}$). The angle θ^* is between the new z-axis and the outgoing lepton (l) and ϕ^* is between the lepton plane and the plane of the incident hadrons.

The angular coefficients, A_0 to A_7, are functions of the invariant mass (M_{ll}), rapidity

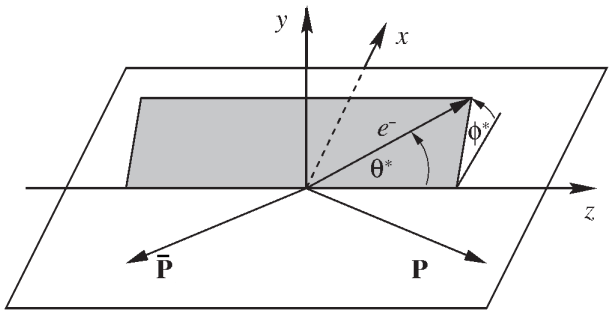

Figure 1.5. Collins-Soper Frame: In the rest frame of the Z boson, the lepton pair is produced back to back, however, in general p and $\bar{p}$ are not collinear

(y), and transverse momentum (p_T) of the dilepton pair in the lab frame. According to perturbative QCD (pQCD), A_0 and A_2 are the same for Z or γ^* exchange and A_3 and A_4 originate from Z/γ^* interference. A_5, A_6, and A_7 are expected to be zero [7]. Also, the A_1 term cancels out during integration.

- Leading order (LO) calculations are sensitive to quark PDFs: Partons carry different momentum fractions, which then affect the rapidity of the produced Z/γ^*.

- At next-to-leading (NLO) order, initial state gluons are included, which also alter the rapidity of the produced Z/γ^*, and thus this measurement gives a test of these calculations

The analysis is performed on five p_T bins, averaged over rapidity. We note that the high p_T region is dominated by perturbation theory, while the low p_T region is calculated using re-summation techniques.

The measurement of angular coefficients describes interesting fundamental physics listed as follows:

- For the annihilation process, pQCD at order of the coupling constant α_s when averaged over y, predicts that the angular coefficients A_0 and A_2 are equal and can be analytically described by $A_0^{q\bar{q}} = A_2^{q\bar{q}} = \dfrac{p_T^2}{(M_{e^+e}^2 + p_T^2)}$.

  For the Compton scattering,

$A_0^{qG} = A_2^{qG} \approx \frac{5p_T^2}{(M_{e^+e}^2 + 5p_T^2)}$.

Fixed order pQCD calculations at NLO indicate significant contribution from Compton scattering ($\approx 30\%$) to the production of Z/γ^* bosons at the Tevatron, implying values of A_0 and A_2 larger than that from a pure annihilation process. In contrast, calculations based on QCD resummation at LO, predicts values of A_0 and A_2 close to that of a pure annihilation process at low p_T and larger values (close to pQCD) at high p_T. Therefore, measurements of A_0 and A_2 as functions of p_T elucidates the relative contribution of annihilation and Compton processes Figure 1.4, and provides a detailed test of the production mechanism of the Z boson.

- The equality $A_0 = A_2$ is known as the Lam-Tung relation and is valid only for vector (spin-1) gluons. Therefore, a confirmation of the Lam-Tung relation is a fundamental test of the vector gluon nature of QCD and is equivalent to the measurement of the spin of the gluon.

- The coefficient A_4 determines forward and backward asymmetry. The Forward-Backward asymmetry arises due to the presence of both vector and axial-vector couplings of the bosons to fermions in $q\bar{q} \rightarrow Z/\gamma^* \rightarrow l^-l^+$ as shown in Figure 1.3. According to the SM, the coupling of a fermion f to the Z boson is $\bar{f}(g_V^f - g_A^f\gamma_5)f$, where g_V^f and g_A^f are the vector and axial-vector couplings of the fermion to the Z, respectively; whereas the coupling of a fermion to the virtual photon (γ^*) is purely a vector coupling. The A_4 coefficient is related to the Forward-Backward asymmetry coefficient A_{fb} as, $A_{fb}(M_{ll}) = \frac{3}{8}A_4$ (derived later in the charge-misidentification section) and is sensitive to the weak mixing angle, $\sin^2\theta_W$. Hence, it can be used to extract $\sin^2\theta_W$ using theory. The $\sin^2\theta_W$ is central parameter of the SM. It determines the relative strengths of the electromagnetic coupling g_e and the weak couplings g_W and g_Z through ($g_w = \frac{g_e}{\sin\theta_W}$ and $g_z = \frac{g_e}{\sin\theta_W\cos\theta_W}$). It also relates the masses of the W and Z bosons

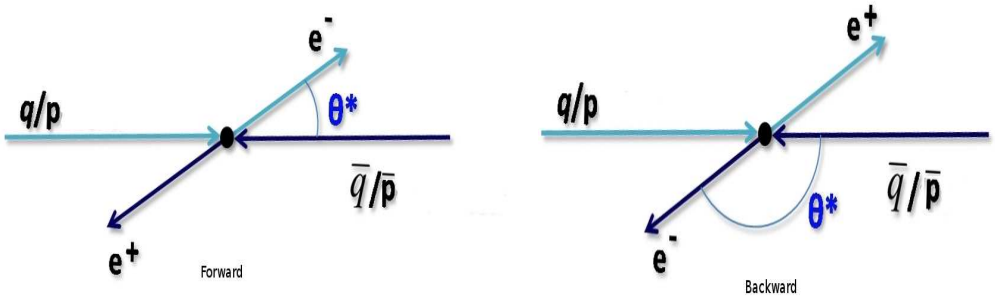

Figure 1.6. Forward events (left), the electron is produced along the direction of incoming proton $\cos\theta^* > 0$. Backward events (right), the electron is produced in opposite direction of incoming proton $\cos\theta^* < 0$.

through $M_W = M_Z \cos\theta_W$.

Chapter 2

Experimental Apparatus

The experimental apparatus is a multi-purpose particle detector called DØ, located at the Tevatron accelerator at the Fermi National Accelerator Laboratory (Fermilab) near Chicago. The Tevatron is a four mile circumference superconducting synchrotron that accelerates beams of p and $\bar{p}$ to nearly the speed of light. The two beams travelling in opposite directions, collide at two different locations around the ring, at center-of-mass energy $\sqrt{s} = 1.96$ TeV. The collision point BØ is the location of the CDF (Collider Detector at Fermilab) experiment, whereas the DØ experiment derives its name from its collision point.

2.1 The Tevatron Accelerator

Fermilab actually uses a series of seven accelerators to boost $p/\bar{p}$ to $\sim$ 1 TeV. The Fermilab accelerator complex is shown in Figure 2.1. The first step is to add electrons to hydrogen gas atoms to produce H^- ions. These ions are accelerated to 750 keV with a Cockcroft-Walton pre-accelerator. The H^- ions are then injected to a 150 m long linear accelerator (LINAC), consisting of radio-frequency (RF) cavities which accelerate the ions to an energy of 400 MeV. A thin carbon foil strips off electrons from the H-ions. The resulting protons are transfered to the Booster ring, a synchrotron which accelerate protons up to 8 GeV.

The Booster delivers protons to the Main Injector. The Main Injector (MI) performs the following four primary functions at the Tevatron Collider.

1. It accelerates protons from 8 GeV to 150 GeV before injecting the beam into the Tevatron.

2. It produces protons of energy 120 GeV and delivers them for $\bar{p}$ production.

3. It contains the Recycler (storehouse for cooling and storing $\bar{p}$'s). The MI receives $\bar{p}$'s from the Recycler and accelerates them to energies of 150 GeV.

4. It injects protons and $\bar{p}$'s into the Tevatron for further acceleration of up to 1 TeV.

The Antiproton Source consists of Debuncher and Accumulator rings. Antiprotons are produced by bombarding a nickel (Ni) target with 120 GeV protons from the MI every 1.5 seconds. The $\bar{p}$'s and other particles produced in th p-Ni collisions are focussed into a beam line by a lithium lens. The $\bar{p}$'s are then separated by sending the beam through a pulsed magnet mass-charge spectrometer. The $\bar{p}$ beam produced has an undesirably large spread in energy but relatively small spread in time.

The Debuncher phase rotates the beam so that it possesses a narrow energy and large time spread. The Debuncher is a triangular RF cavity ring. It recieves low energy $\bar{p}$'s at a different phase of the RF than the high energy ones, due to the different path lenghts travelled around the ring. The difference in phase causes low energy particles to be accelerated, while the high energy ones get decelerated. Thus, the $\bar{p}$'s are gradually "debunched", meaning the temporal spread is increased, while the energy spread is decreased. The $\bar{p}$ beam is then moved to the Accumlator, making space for the next incoming pulse. The Accumulator is capable of cooling and storing the $\bar{p}$ beam over many hours. It also transfers the $\bar{p}$'s to the Recycler periodically, for additional cooling and accumulation.

Upon adequate accumulation of p's and $\bar{p}$'s and consequent acceleration up to energies of 150 GeV at the Main Injector, both of the beams are transfered to the Tevatron. The Tevatron has more than 1,000 superconducting magnets (dipoles and quadrupoles), cooled by liquid helium to -268° Celsius. They produce magnetic fields much stronger than those of conventional magnets, and they help bend, focus, and steer the beams around the ring. The beams are accelerated further, up to energies of 1 TeV each, before allowing them to

collide at the center of the two detectors, CDF and DØ. The collisions occur every 396 ns at a center-of-mass energy of $\sqrt{s} = 1.96$ TeV. Figure 2.1 shows the layout of the different accelerators in the chain and their contributions to the production and acceleration of the p's and $\bar{p}$'s, at the various stages.

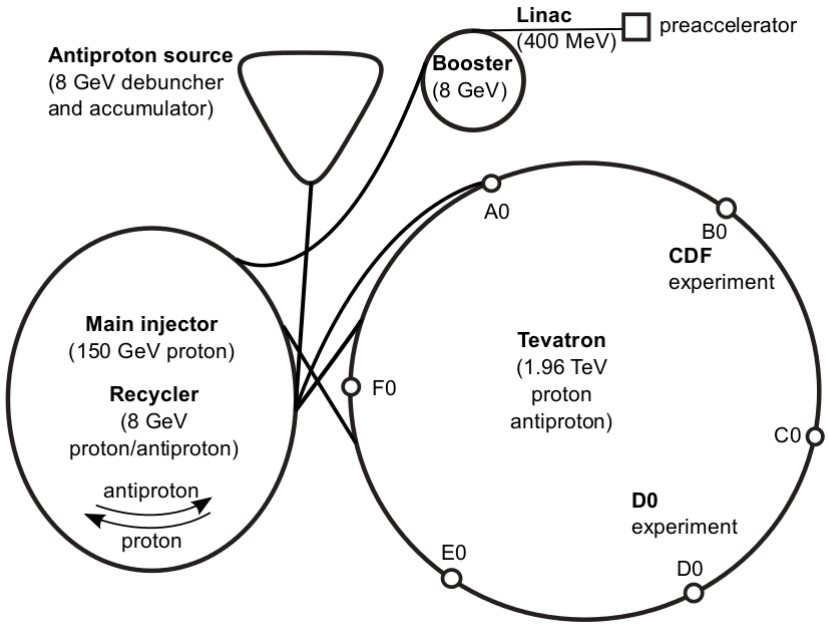

Figure 2.1. Schematic diagram of the Fermilab's accelerator chain

2.2 The DØ detector

The DØ detector, Figure 2.2, is a 5,000-ton multipurpose particle detector used to study fundamental interactions. It works on the same principle as a camera, by taking snapshots of the debris coming out of high energy p-$\bar{p}$ collisions. A more detailed description of the Run II DØ detector from a construction and technical point of view, can be found in reference.[8]

The centeral tracker has two main components, the Silicon Microstrip Tracker (SMT) and the Central Fibre Tracker (CFT), located inside a 2 Tesla magnetic field provided by a superconducting solenoid. It is used for position and momentum measurement of charged particles. The tracking system is surrounded by two scintillators based Central (CPS) and

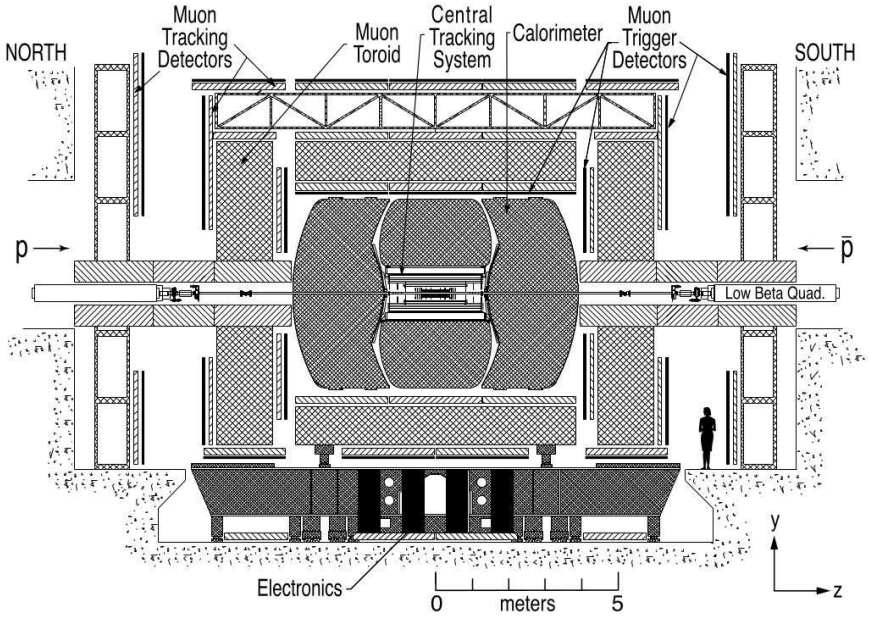

Figure 2.2. A view of the DØ Run II upgraded detector.

Forward (FPS) Preshower detectors to provide electron identification. The Calorimeter is made of five sampling Uranium-liquid Argon cryostats: a central cryostat covering the region $|\eta| < 1.2$, two forward cryostats extending the coverage to $|\eta| < 4$ and two Inter Cryostat Detectors to cover the overlapping pseudorapidity region. A Muon system resides beyond the calorimetry, and consists of a layer of tracking detectors and scintillation trigger counters before a 1.8 Tesla toroid, followed by two more similar layers after the toroid. Luminosity is measured using plastic scintillators arrays located in front of the Electromagnetic Calorimeter (EC) cryostats. The three-tiered trigger and data-acquisition is designed to accommodate the high luminosities of Run II.

2.2.1 Central Tracking System

Inner tracking as shown in Figure 2.4, includes the Silicon Microstrip Tracker (SMT) and the Central Fibre Tracker (CFT) inside a 2 T solenoidal magnet.

- **The Silicon Microstrip Tracker** The silicon tracking system as shown in Figure 2.3, is based on 50μm pitch silicon microstrip detectors, with a total of 793,000 channels,

and provides a spatial resolution of approximately 10μm in $r\phi$. The high resolution is important to obtain good momentum measurement and vertex reconstruction. The detector consists of a system of six barrels and interspersed twelve disks so-called 'F-disks'. Two (originally four) large radius detectors, so-called 'H-disks', are located at the ends of the detector to enhance tracking at very large pseudo-rapidities $|\eta| < 3$. The barrels provide tracking for particles with high transverse momentum in the central regions $|\eta| < 1.5$, while the disk detectors allow for the precise reconstruction of particles traveling with pseudo-rapidity up to $|\eta| < 3$. The SVXIIe chip is used for readout.

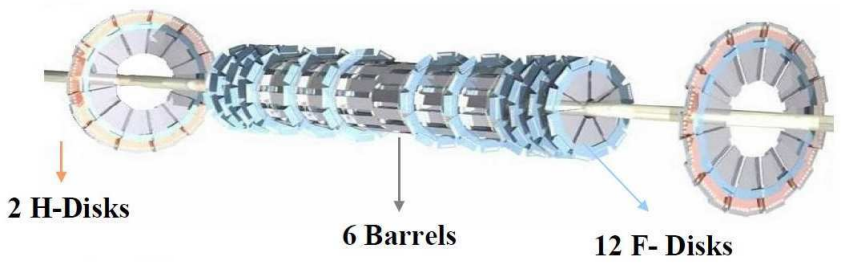

Figure 2.3. Layout of the SMT. The barrels, F-disks and H-disks are labelled.

- **The Central Fibre Tracker** The detector just outside the SMT is the 8-layered CFT, which is based on scintillating fiber ribbon doublets with visible light photon counter (VLPC) readout [8]. On average, an ionizing charged particle produces about ten photons. The wavelength shifting optical fibres transport light to VLPCs, which convert these photons to electrical pulses. The combined hit information from the SMT and CFT allows good track reconstruction and momentum determination for the region up to $|\eta| < 1.7$.

2.2.2 Calorimeter

A typical calorimeter provides a measurement of the energy of energetic particles like photons, electrons, and hadronic jets. The energetic particles passing through a large amount

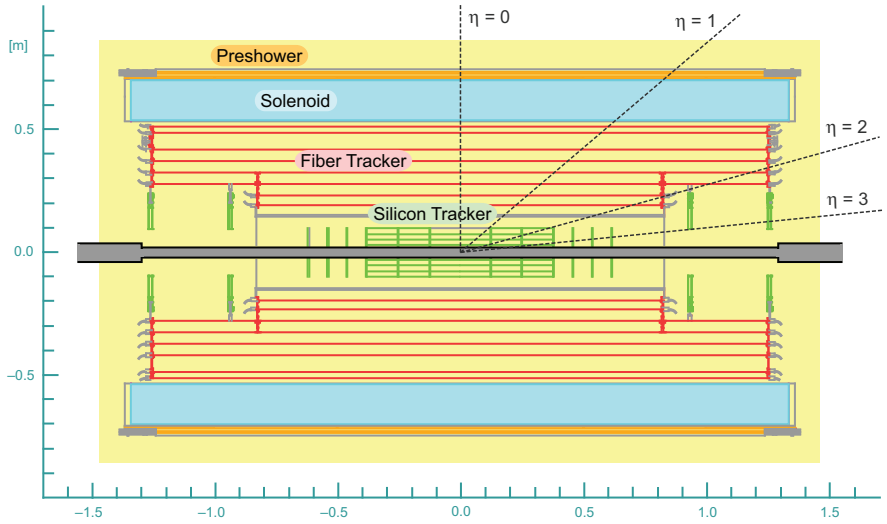

Figure 2.4. DØ tracking detector

of dense material create showers of energy which are then absorbed by surrounding active material. The DØ calorimeter, figure 2.5, is a compensating sampling calorimeter with fine segmentation. It uses liquid argon (LAr) as an active medium and depleted uranium, stainless steel/copper plates as absorber materials. In a sampling calorimeter, the shower development of the incident particles is periodically sampled via the ionization of an active medium. By compensating, it is meant that the ratio of the electromagnetic and hadronic response (e/h) is close to one. Calorimeter segmentation in the transverse and longitudinal shower directions, allows one to measure the shape of the shower development and determine the direction of the incident particles which helps in the identification of different types of particles such as electrons, photons and hadrons. There are three liquid argon calorimeters housed in three separate cryostats - one central (CC) (with $|\eta| < 1.1$) and two endcaps (EC) (with $1.5 < |\eta| < 4.2$). In the inter-cryostat region ($1.1 < |\eta| < 1.4$), both "massless gaps" and an inter-cryostat detector (ICD) have been added to sample the shower energy that is lost by particles that transverse the module endplates and cryostat walls. Each calorimeter module is further segmented into three distinct sections. In order of increasing radius, these are: Electromagnetic (EM) section with relatively thin uranium

absorber plates, fine-hadronic (FH) with thick uranium plates, coarse-hadronic (CH) with thick copper or stainless steel plates.

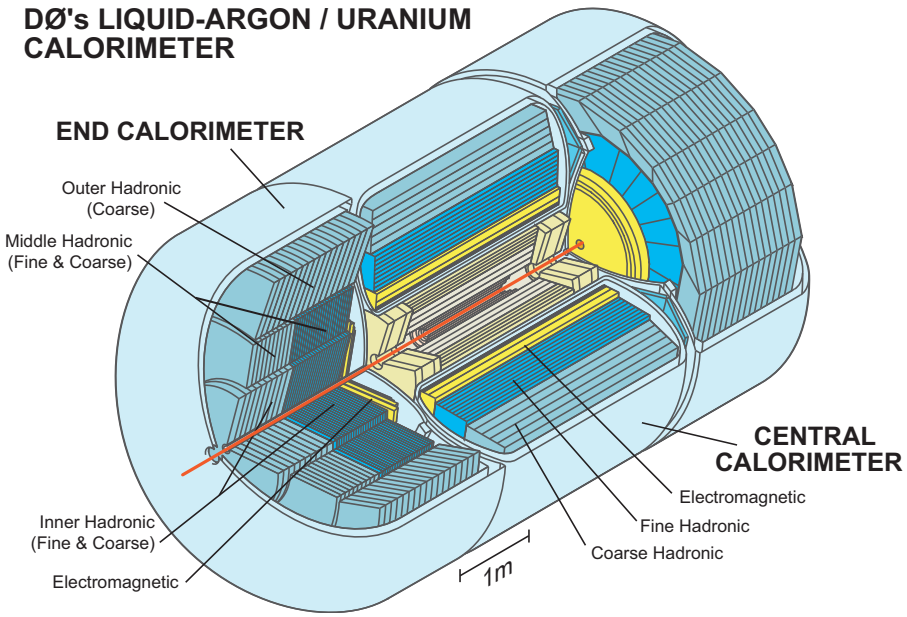

Figure 2.5. Cut away view of the calorimeter. The three cryostats, and the different layers (electromagnetic, fine and coarse hadronic) are labelled.

2.2.3 Muon System

The calorimeter is surrounded by the muon system. It is designed to detect the passage of muons as well as measure their momenta. Due to its large mass ($\sim$ 200 $m_{electron}$), a muons loses little energy via bremsstrahlung at Tevatron energies (i.e., they do not readily initiate electromagnetic showers). Energy loss for muons occurs primarily via ionization and excitation of the detector media, which are low energy-loss absorption processes. Therefore, muons above some energy threshold ($\sim 3.5 - 5.0$ GeV) can escape the calorimeter. Hence, the muon system is typically the outermost and physically the largest detector system. Being located outside the calorimeter, the muon system is well protected from the debris from the hadronic and electromagnetic showers by the thick calorimeter material. Thus, muons can be identified in the middle of hadron jets with much greater purity than electrons.

2.2.4 Trigger System

Triggering is an essential part of a high luminosity high energy physics experiments as it is of great importance not to lose rare events over the common ones. Fast decisions and cuts are therefore crucial, although they can lead to biases due to finite (and often worse) resolution of the trigger-level object. The DØ trigger and DAQ systems have been completely upgraded to handle the shorter bunch spacing and new detector subsystems in RunII. The level 1 and 2 triggers utilize information from the calorimeter, preshower detectors, central fiber tracker, and muon detectors. The level 1 trigger reduces the event rate from 7.5 MHz to 10 kHz and has a latency of 4 μs. The trigger information is refined at the level 2 trigger using calorimeter clustering and detailed matching of objects from different subdetectors. The level 2 trigger has an accept rate of 1 kHz and a latency of 100 μs. Level 3, consisting of an array of PC processors, partially reconstructs event data within 50 msec to reduce the rate to 50 Hz. Events are then written to tape.

Chapter 3

Analysis technique

This analysis focuses on the electron channel. The good energy resolution and angular acceptance of electrons at DØ helps in selection of a clean $Z \rightarrow e^+e^-$ sample with low background. The following are main steps for the measurement:

- We start by selecting a clean sample of $Z \rightarrow e^+e^-$ events by applying suitable selection cuts;
- Monte Carlo (MC) tuning:
  - Apply efficiency corrections;
  - Apply charge Mis-identification corrections;
  - Apply energy scale and resolution corrections;
- Estimate and subtract residual QCD and other SM backgrounds;
- Measure/Extract the value of A_i's using a template fit method.
- Estimate systematic uncertainities.

3.1 Event Selection

In order to accept the maximum number of signal events as well as reduce the background as much as possible, we apply selection cuts on data sets. These cuts or selection criteria

ensure that the selected events are as good as possible. The selection cuts are optimized to select two high p_T electrons from Z boson decay.

We select two electrons with high transverse momentum, $p_T^{EM} > 25$ GeV found either in the CC or EC region of calorimeter. The fiducial requirement avoids cryostat edges and removes electron candidates near the ϕ gaps due to module boundaries as well as calorimeter areas that have an identified hardware problem. The sum of invariant mass (M_{ee}) of the selected e^+e^- pair should be near the Z peak ($60 < M_{ee} < 130$ GeV) region, insuring we select $Z \to e^+e^-$events only. The coordinate of the lepton origin along the beam line (z direction) must fall within 40 cm of the center of the detector at distance of closest approach (DCA) to ensure a good energy measurement in the calorimeter.

Tight electromagnetic identification (EM ID) cuts along with the DCA tracking requirement get rid of most fake electrons. The two variables, EM fraction and isolation are used as the main criteria for identifying electromagnetic candidates. A high value of the EM fraction f_{EM} indicates that most of the energy of the shower is contained in the four EM layers of the calorimeter. The fraction of the electron energy deposited in the 4 electromagnetic (EM) layers of the calorimeter is required to be greater than 90%.

The isolation variable f_{iso} , is a measure of how well the energy cluster is isolated from other objects such as hadronic jets and is defined as

$$f_{iso} = \frac{E_{Tot}(0.4) - E_{EM}(0.2)}{E_{EM}(0.2)}.$$

A well reconstucted electron is isolated in calorimeter, with most of its energy deposited in a cone of radius $\Delta R = \sqrt{(\Delta\phi)^2 + (\Delta\eta)^2} = 0.2$. We require isolation to be at least 0.15.

Track Isolation is defined as scalar sum of transverse momentum (p_T) of all tracks, originating from the interaction point in an annulus of $\Delta R(0.05, 0.4)$ around the EM cluster. We require it only for the EC region, where $p_{T,trk}^{sum} = \Sigma p_{T,trk} < 2.50$ GeV.

3.2 Simulation

In addition to real data, experiments in particle physics use event simulations to predict what events of interest look like in the detector. Monte Carlo (MC) event generators are used to produce simulations of expected signal as well as background processes. A MC is a computer code, capable of simulating highly energetic events such as those actually produced in particle accelerators of collider experiments. An "event" is a list of particles (mesons, hadrons, etc.) along with their energies and momenta, produced by $p\bar{p}$ collisions. First, events are generated based on information from a theoretical model in order to correctly predict the final state that could arise from the collisions. Then, events are processed through a model of the detector which simulate the detector response. Finally, processed events are reconstructed just like the data coming out of the detector.

At DØ the Common Samples Group (CSG) generates and provides all the MC samples for different analysises. The $p\bar{p}$ interaction is simulated using programs like ALPGEN + PYTHIA , or PYTHIA [9]. The DØ detector is modeled using the GEANT package.

3.3 Efficiency Studies

There is always some disagreement between data and MC because we cannot simulate all the detector effects. Therefore, the number of events passing a given selection cut is different in data from that in MC. Efficiency is defined as the fraction of events passing a given selection cut. To make MC agree with the data, we derive scale factors (or correction factors) which are the ratio of efficiency of Data and that of MC.

Tag and probe is a general technique to calculate efficiencies and derive scale factors. One uses a mass resonance decaying into a di-object, for example, $Z \to e^+e^-$. A lepton candidate, which satisfies the trigger criteria, tight identification, and isolation requirements is selected and called the "tag". Tight selection reduces the amount of background and makes sure we get a well reconstructed electron with low fake rate (less jet contamination). Then the other lepton candidate, is paired to the selected tag by requiring some loose criteria

and is selected as the "probe". To increase the probability that the selected event is really a boson decay event, we require the reconstructed mass of tag and probe to be close to the Z boson. "Passing probe" is a subset of the probe set and is required to pass a specific criteria which depends on the efficiency (identification or tracking) under study. The efficiency is defined as the fraction of "passing probe" leptons which pass the selection criteria under study.

$$\epsilon(probe) = \frac{N_{\text{passing probes}}}{N_{\text{all probes}}}$$

The scale (correction) factors for the simulation are the ratio of efficiency of data to that of MC,

$$\rho_{eff} = \frac{\epsilon_{data}}{\epsilon_{MC}}$$

Consider $Z \to e^+e^-$events, each EM object (electron) can be identifed based on its signature in the tracker and calorimeter.

- **Tag Selection** Tag selection is the same for both electromagnetic identification and tracking efficiency and for the central or end-cap region of the calorimeter. A tag is selected using both electomagnetic cluster and tracking information. We select a high-p_T electron in a well instrumented (both η and ϕ fiducial) region of central calorimeter. The fiducial requirement avoids cryostat edges and removes electron candidates near the ϕ gaps due to module boundaries as well as calorimeter areas that have an identified hardware problem. The coordinate of the lepton, along the beam line (z direction) must fall within 40 cm of the center of the detector at distance of closest approach (DCA) to ensure a good energy measurement in the calorimeter. Tight electromagnetic identification (EM ID) cuts along with tracking requirements gets rid of most fake electrons

- **Probe Selection** After the selection of high-p_T leptons as Tag, we get rid of most fake electrons and get a high purity Z sample. The second electron (Probe) is considered

separately in the central and end-cap regions of the calorimeter. For each region we perform both EM identification and tracking study.

Electomagnetic Identification

* For EM identifiaction efficiency in the central region, the probe is selected based on tracking and geometric criteria. The track associated with the probe is paired with the selected Tag. Additionally, we cut on invariant track mass ($M_{\text{Tag, Probe}}$), which must be around resonance mass (Z_{mass}) to select only $Z \rightarrow e^{+}e^{-}$ events. Only the tracking information and no EM identification is used without even requiring it to be an electron (in order to avoid bias during selection). Figure 3.11 shows the EM ID efficiency of data (blue), Monte-Carlo (red) vs electron p_T and scale factors vs electron p_T in the central calorimeter region for Run IIb2.
* For probe in the End Cap region, we do not require a track match for EM identification. This is because the forward region has limited central fiber tracker coverage. Figure 3.3 shows the EM ID efficiency of data (blue), Monte-Carlo (red) vs electron p_T and scale factors vs electron p_T in the end cap region of the calorimeter for Run IIb2.

Tracking efficiency

* For tracking efficiency in the central calorimeter region, probes are selected with momentum greater than 20 GeV/c. The invariant mass of tag and probe candidates should be around the Z peak. The tag and probe must be back-to-back in order to reduce jet background. Also, the "passing probe" must have a track with finite tracking probability. Figure 3.2 shows tracking efficiency of data (blue), Monte-Carlo (red) vs electron p_T and scale factors vs electron p_T in the central calorimeter for Run IIb2.

* Depending on the CFT tracking coverage we divide the EC tracking efficiency into three categories. Splitting data in to types allows us to choose specific cuts for each type that improves charge identification while maintaining high statistics. For each type, we have different selection cuts and measure the track efficiency separately. Figures 3.4, 3.5, and 3.6 show the tracking efficiency of data (blue), Monte-Carlo (red) vs electron p_T and scale factors vs electron p_T in the end cap region of the calorimeter for Run IIb2 for type 2, 3, and 4, respectively.

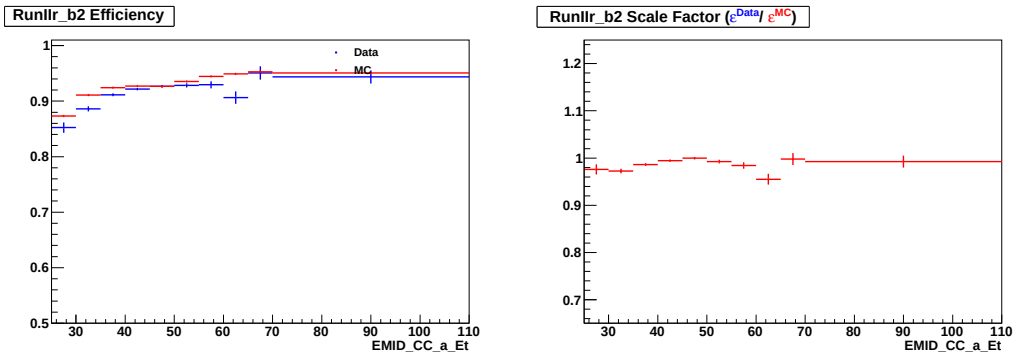

Figure 3.1. Left: EM ID efficiency of data (blue), Monte-Carlo (red) vs electron p_T . Right: scale factors vs electron p_T in CC for Run IIb2.

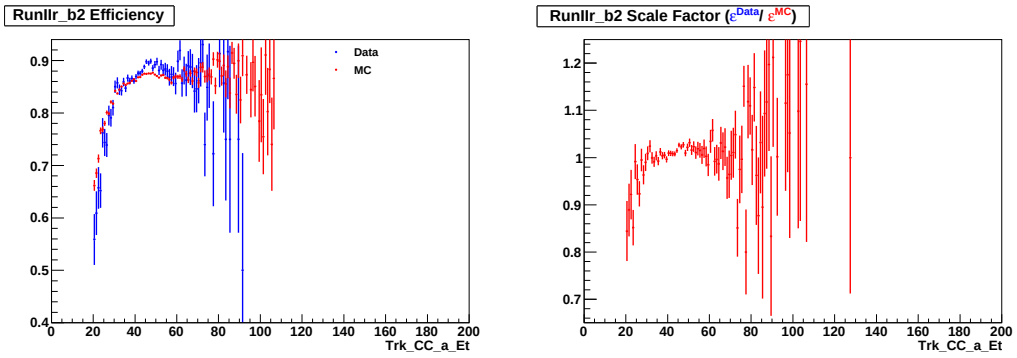

Figure 3.2. Left: Tracking efficiency of data (blue), Monte-Carlo (red) vs electron p_T . Right: scale factors vs electron p_T in CC for Run IIb2.

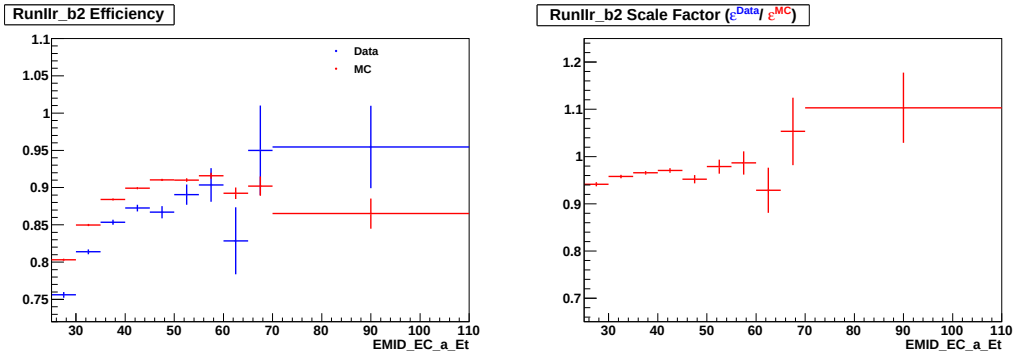

Figure 3.3. Left: EM ID efficiency of data (blue), Monte-Carlo (red) vs electron p_T . Right: scale factors vs electron p_T in EC for Run IIb2.

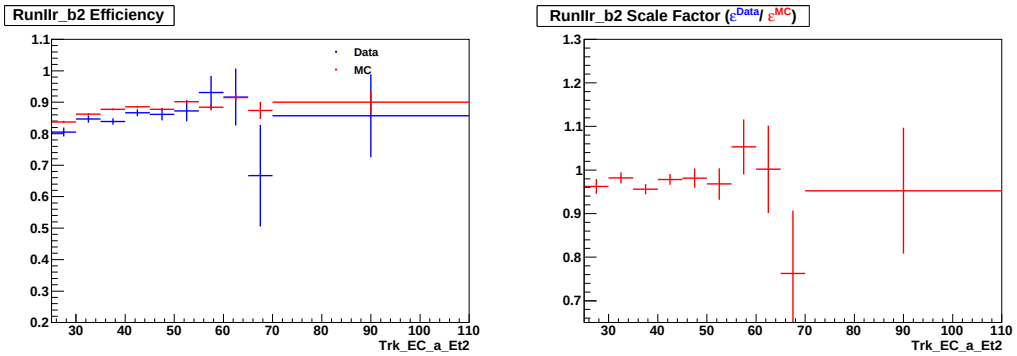

Figure 3.4. Left: Tracking efficiency (type 2 electorns) of data (blue), Monte-Carlo (red) vs electron p_T . Right: scale factors vs electron p_T in EC for Run IIb2.

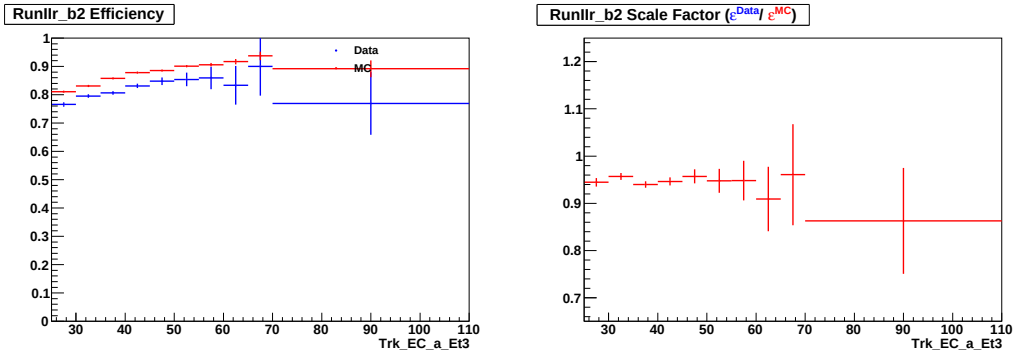

Figure 3.5. Left: Tracking efficiency (type 3 electorns) of data (blue), Monte-Carlo (red) vs electron p_T . Right: scale factors vs electron p_T in EC for Run IIb2.

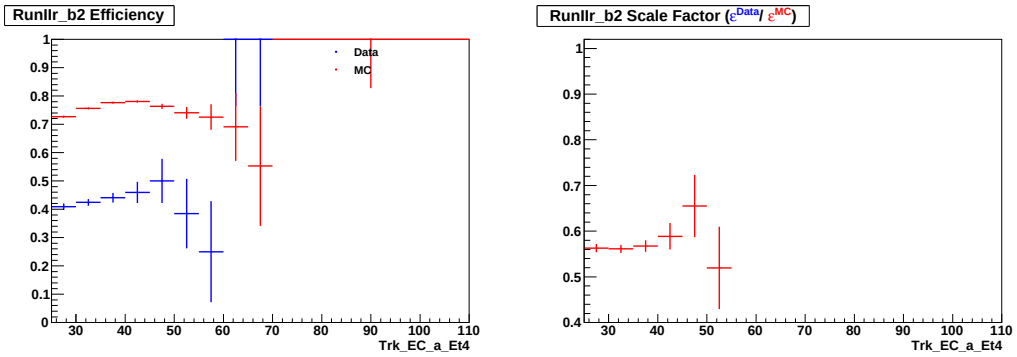

Figure 3.6. Left: Tracking efficiency (type 4 electorns) of data (blue), Monte-Carlo (red) vs electron p_T . Right: scale factors vs electron p_T in EC for Run IIb2.

3.4 Charge Mis-identification

The charge mis-identification rate (f_Q) is the probability that a real electron will be an assigned incorrect charge. We measure it by checking the charge on both leptons selected by passing through standard selection cuts. If the charge of both the leptons are the same, we say the charge was mis-identified. If they are opposite, then we say it was identified correctly.

The angular distribution is sensitive to the charge of the lepton. The Collins-Soper angle θ^* (Figure 1.5) is defined with respect to outgoing negative lepton (electron). We get the charge information of the lepton from its track and determine whether the selected lepton is an electron or positron, then use the four vectors to calculate $\cos\theta^*$. The charge mis-identification only effects the A_4 coefficient (as noted in Eq. (1.5)). Since the charge mis-identification rate is very small $\sim .2 - .4\%$, its effect is negligible on A_0 which has the $(1 - 3\cos^2\theta^*)$ term.

The charge mis-identification rate (or fake rate) is defined as

$$f_Q = \frac{1}{2}\frac{N_{SS}}{N_{OS} + N_{SS}},$$

where, N_{SS} are events with both leptons having same signs and N_{OS} are those with opposite sign leptons. Depending on the location inside the detector, we classify our dilepton event into three different cases. The CC-CC (or EC-EC) event when both leptons are in central (or end cap) region of calorimeter. The CC-EC event when one electron is in CC region and the other is in EC region. For CC-CC event, we require that the two EM clusters must have an opposite charge. Thus, the probability (or fake rate, f_Q) to identify forward event as backward event, and vice versa, is small. Lack of tracking coverage for EC region makes mis-identification rate higher for CC-EC and EC-EC events.

- For a CC-CC event, $A_4^{meas} = \frac{(1-2f_Q)}{(1-2f_Q+2f_Q^2)} A_4^{true}$.

- For both CC-EC and EC-EC events, $A_4^{meas} = (1 - 2f_Q)A_4^{true}$.

Depending on case, CC-CC or CC-EC or EC-EC, the f_Q has different values.

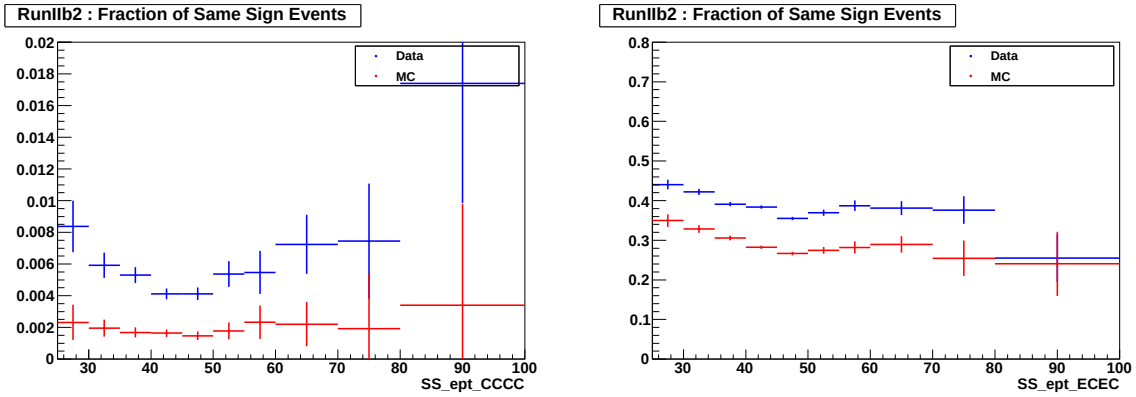

Figure 3.7. Charge mis-identification rate for electron p_T (Run IIb2)

3.5 Background Estimation

While selection cuts get rid of most of the background, our sample is still not 100% pure. For example, both the photon and electron have the same shower shape, except that the former do not leave tracks in tracking detector. However, due to instrumental noise, a photon can be mis-identified as an electron. In the following Standard Model (SM) processes, two electrons or photons or jets in final state can be identified as $Z \to e^+e^-$events and contribute as sources of background to $p\bar{p} \to Z/\gamma^* + X \to e^+e^- + X$, which are listed below.

- QCD: dijets events misidentified as electons, measured from data.
- $W + X \to e\nu + X$, X is a jet or γ misidentified as an electron.
- $Z/\gamma^* \to \tau^+\tau^- \to e^+e^-\nu_\tau\nu_e\bar{\nu}_\tau\bar{\nu}_e$
- $t\bar{t} \to Wb + W\bar{b} \to e\nu b + e\nu\bar{b}$
- Dibosons
  - $\gamma + \gamma$, where γ misidentified as electon.

* $W^+W^- \rightarrow e^+e^-\nu_{e^+}\nu_{e^-}$

* $W^{\pm}Z$

* ZZ

The QCD (or instrumental) background, where jets are mis-reconstructed as electrons, is the dominant source of background. It is measured using real data by inverting the shower shape requirement of electrons and removing the electron track matching cuts. $W + X$, where X is a jet or photon mis-identified as an electron is the second largest source of background. Comparision studies between ALPGEN + PYTHIA and PYTHIA generators for W+X estimation were performed. We observed that PYTHIA over-estimates the W+X contribution compared to ALPGEN + PYTHIA . Hence, it was decided to use the ALPGEN + PYTHIA MC generator combined with GEANT simulation of the DØ detector to estimate W+X. All the other backgrounds are measured using the PYTHIA MC generator tuned with detector simulation and are mostly negligible. Figure 3.8, shows comparisions between data and signal+QCD+EW background events.

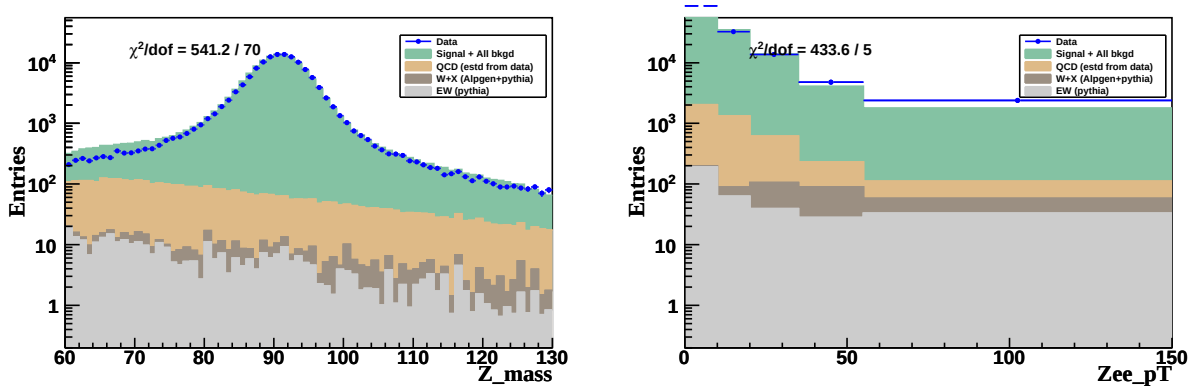

Figure 3.8. Invariant mass (left), Z p_T (right) distribution for RunIIb2 data. Signal and background for All regions.

p_T Bins	W + X (alpgen + pythia)	Sum ($\gamma + jets$) (pythia)	W +γ (pythia)	W + Jets (pythia)
$0 - 10$	8.083 ± 1.911	17.078 ± 2.993	3.925 ± 0.130	13.152 ± 2.990
$10 - 20$	26.103 ± 4.040	39.149 ± 4.592	11.094 ± 0.217	28.055 ± 4.587
$20 - 35$	66.047 ± 6.452	81.472 ± 6.562	26.170 ± 0.338	55.303 ± 6.553
$35 - 55$	61.742 ± 6.521	82.284 ± 6.603	22.640 ± 0.313	59.645 ± 6.595
$55 - 150$	24.886 ± 3.648	29.670 ± 4.323	7.565 ± 0.180	22.105 ± 4.319

Table 3.1. alpgen + pythia vs pythia : Z_{p_T} in 5 p_T bins for all regions.

3.6 PYTHIA vs ALPGEN + PYTHIA for $W + X$

The $W + X \to e\nu + X$, where X is the jet or γ mis-identified as electron is the second dominant source of the background. Figure 3.9 shows that the Collins-Soper $\cos\theta^*$ and ϕ^* distribution comparisions between ALPGEN + PYTHIA and PYTHIA Monte-Carlo generators.

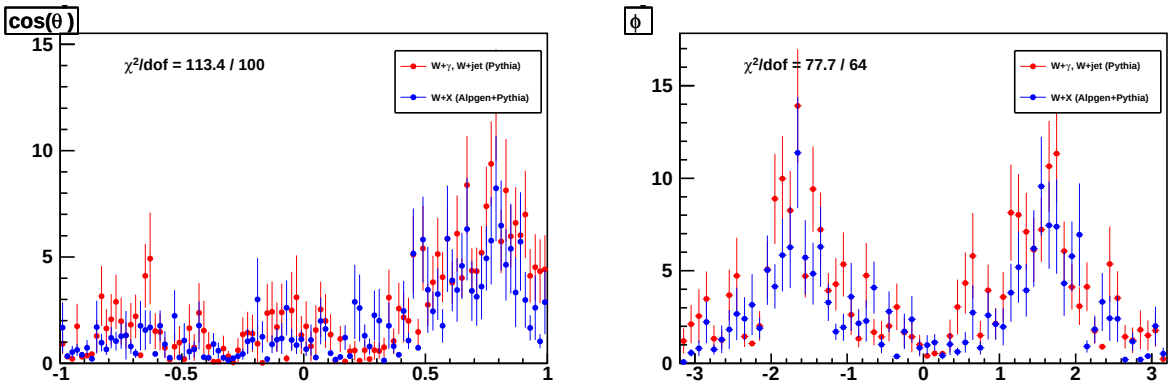

Figure 3.9. The Collins-Soper $\cos\theta^*$ and ϕ^* distribution for W+X background

The Figures 3.10 shows the Z_{p_T} distribution in 5 p_T bins for all, CC-CC, CC-EC and EC-EC calorimeter region and tables 3.1,3.2, 3.3, 3.4 summarizes the ALPGEN + PYTHIA and PYTHIA estmation of W+X backgrounds. We observe that PYTHIA over-estimates the W+X contribution compared to ALPGEN + PYTHIA .

3.7 Extraction of Coefficients

We use an analytic fit method to extract the values of angular coefficients from data, by comparing it with the reweighted MC. The following steps are involved in getting the final

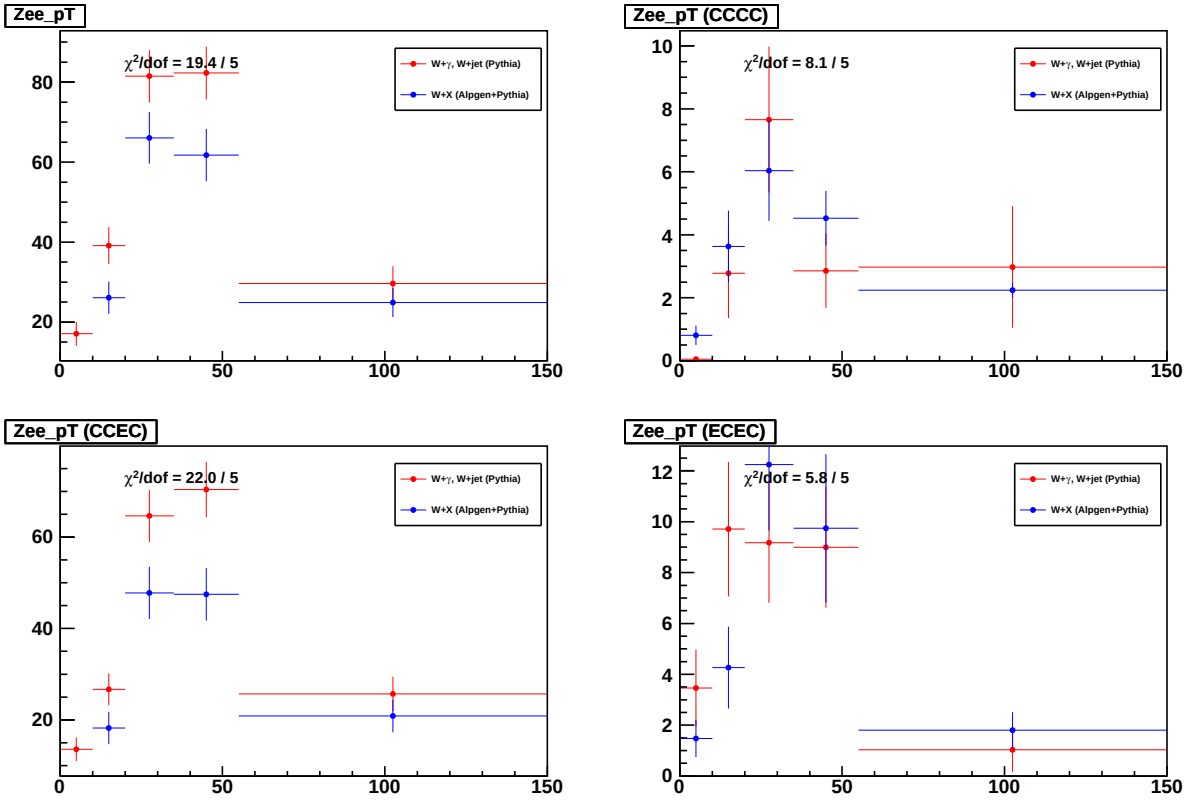

Figure 3.10. Comparison between alpgen + pythia and pythia for W+X background: Top left shows Z_{p_T} in 5 p_T bins for All calorimeter region, top-right corresponds to CCCC region and bottom left (right) shows the same distribution for CCEC (ECEC) regions.

p_T Bins	W + X (alpgen + pythia)	Sum ($\gamma + jets$) (pythia)	W +γ (pythia)	W + Jets (pythia)
$0 - 10$	0.808 ± 0.309	0.046 ± 0.014	0.046 ± 0.014	0.000 ± 0.000
$10 - 20$	3.630 ± 1.137	2.775 ± 1.425	0.142 ± 0.028	2.633 ± 1.424
$20 - 35$	6.033 ± 1.589	7.658 ± 2.317	0.302 ± 0.037	7.356 ± 2.317
$35 - 55$	4.522 ± 0.869	2.854 ± 1.189	0.205 ± 0.029	2.649 ± 1.189
$55 - 150$	2.242 ± 0.246	2.977 ± 1.933	0.066 ± 0.017	2.911 ± 1.933

Table 3.2. alpgen + pythia vs pythia : Z_{p_T} in 5 p_T bins for CCCC regions.

p_T Bins	W + X (alpgen + pythia)	Sum ($\gamma + jets$) (pythia)	W +γ (pythia)	W + Jets (pythia)
$0 - 10$	5.796 ± 1.736	13.572 ± 2.587	3.668 ± 0.126	9.904 ± 2.583
$10 - 20$	18.211 ± 3.528	26.665 ± 3.473	10.240 ± 0.209	16.425 ± 3.466
$20 - 35$	47.767 ± 5.692	64.636 ± 5.665	23.752 ± 0.324	40.884 ± 5.656
$35 - 55$	47.477 ± 5.768	70.434 ± 6.045	21.339 ± 0.305	49.095 ± 6.037
$55 - 150$	20.843 ± 3.570	25.657 ± 3.766	7.341 ± 0.177	18.316 ± 3.762

Table 3.3. alpgen + pythia vs pythia : Z_{p_T} in 5 p_T bins for CCEC regions.

p_T **Bins**	**W + X** (**alpgen + pythia**)	**Sum** ($\gamma + jets$) (**pythia**)	**W** $+\gamma$ (**pythia**)	**W + Jets** (**pythia**)
$0 - 10$	1.479 ± 0.736	3.460 ± 1.506	0.212 ± 0.029	3.249 ± 1.506
$10 - 20$	4.262 ± 1.607	9.709 ± 2.645	0.712 ± 0.053	8.996 ± 2.645
$20 - 35$	12.248 ± 2.589	9.179 ± 2.366	2.116 ± 0.089	7.063 ± 2.364
$35 - 55$	9.743 ± 2.916	8.997 ± 2.376	1.096 ± 0.065	7.901 ± 2.375
$55 - 150$	1.801 ± 0.712	1.036 ± 0.878	0.158 ± 0.023	0.878 ± 0.878

Table 3.4. alpgen + pythia vs pythia : Z_{p_T} **in 5** p_T **bins for ECEC regions.**

results [10], [11]:

Step 1 Generator level predictions: We start by calculating the default A_i^o's using PYTHIA MC by fitting it to a functional form (equations (1.5) and (1.6)) at the generator level.

Step 2 Reweight MC: Next, we vary one A_i keeping all other coefficients fixed at predicted values (A_i^o's from Step 1) and calculate weight-factors per event per A_i' value,

$$weight = \frac{\frac{d\sigma}{d\cos\theta^*}(A_0', A_4')}{\frac{d\sigma}{d\cos\theta^*}(A_0^o, A_4^o)} or \frac{\frac{d\sigma}{d\phi^*}(A_2', A_3')}{\frac{d\sigma}{d\phi^*}(A_2^o, A_3^o)}$$

Step 3 Generate Templates: Then we apply these weight factors to the MC at reconstruction level and generate the $\cos\theta^*$ and ϕ^* distribution templates corresponding to the different values of A_i.

Step 4 Finally, we compare the reconstruction level Monte-Carlo templates with that of Data and use Min-χ^2 to extract the best values for A_0, A_4 from $\cos\theta^*$ and A_2, A_3 from ϕ^* using minimum χ^2 fit in five separate p_T bins, (0, 10, 20, 35, 55, 150) GeV/c.

3.8 Future Work

3.8.1 Energy Scale and Resolution

MC cannot be expected to reproduce all the features of data from a real detector. For example, it is very difficult to simulate accurately all the real detector effects such as energy

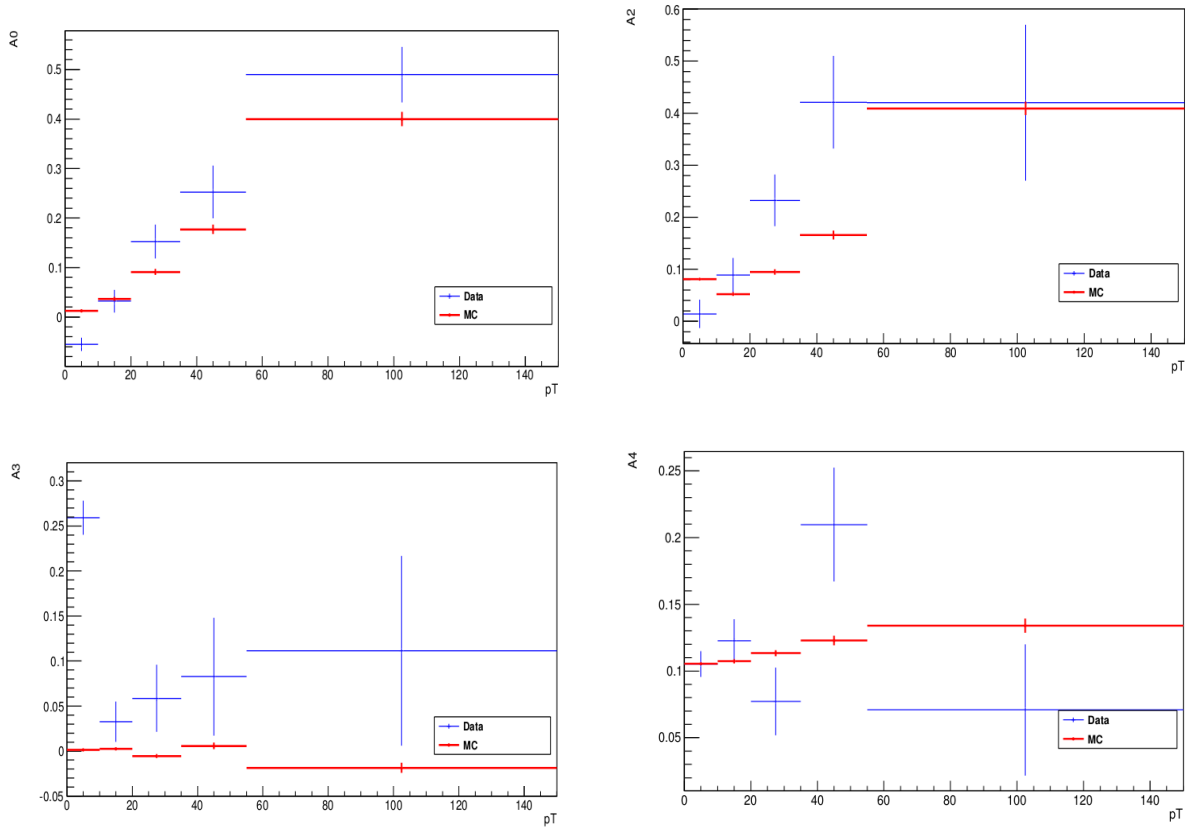

Figure 3.11. Comparison of the measured values of A_0 , A_2 , A_3 , and A_4, for RunIIb2 data. The data (blue) and MC (red) are plotted at the mean p_T of the events for each bin.

loss in dead material (e.g. electronics in front of the calorimeter). As a result, both the position and the width of Z peak in MC is shifted from that in data. For this reason, the electron cluster energy in the MC is smeared to reproduce the resolution in data, and a scale factor (multiplicative correction factor α) is applied to shift the peak location.

The Energy after scaling (E') is,

$$E' = \alpha \times E^{MC},$$

and the additional EM smearing is done using the following formula:

$$E^{smear} = E'(1 + c \times x).$$

Where E^{MC} is the raw energy from the GEANT MC simulation and E^{smear} is the energy after scaling and smearing. α and c are the energy scaling and smearing parameters (CC and EC electrons have different α and c factors) to be found, and x is a random number generated with a Gaussian distribution with zero mean and unit sigma.

Besides mismodeling of energy in the MC, we also expect imperfect detector respose. Hence, we need to perform energy tuning for data as well. The detector has its limitations which effect both the position and width of the Z peak. For example, not all of the energy confined inside the calorimeter cluster is absorbed. After having a good agreement between data and MC, we do a background estimation again. The next step is to extract the values of coefficients.

3.9 Systematic Uncertainities

Due to large statistics, the dominant uncertainty on our measurement will be due to systematics. Our systematics are affected by the experimental uncertainties including: the estimation of background, the energy scale and resolution, the electron identification efficiency, charge mis-identification and material modeling and the theoretical uncertainties like

the boson p_T and rapidity modeling. We will consider the systematic uncertainties in $\cos\theta$ and ϕ distributions for different p_T bins. Since, the $\cos\theta$ depends on the charge measurement, we expect charge mis-identification to be the dominant source of uncertainity.

Chapter 4

Summary

The measurement is to be performed on the entire Run II dataset correspoding to an integrated luminosity of 9.7 fb^{-1} collected at DØ. The data and Monte Carlo (MC) samples were skimmed to select $Z \to e^+e^-$events. We have already finished work on the electron identification efficiency studies using the tag and probe method, of background estimation and charge mis-identification. We still see some data/MC disagreement, which we hope to see disappear once energy scale and resolution correction factors are applied.

We have two more analysis in progress on the same dataset measuring rapidity and forward-backward asymmetry for the Z boson, which are working at a more advanced stage. They have developed a method for electron energy tuning and also have made many cross-checks. We need to put together all the corrections and scale factors to get rid of residual data/MC disagreement. We expect to implement energy correction by the end of August 2013. Also, we have developed and tested inital code for the extraction of angular coefficients. Finalizing and running the code is expected to be finished by the end of September 2013. Further work is needed to be done to estimate systematic uncertainties, which is planned to be finished by the end of October. With help of other analysis on the same dataset, we expect to have final results by mid November of this year. We plan to finish writing the analysis note, get editorial reviews done by the end of the year, and have a publication draft ready by January 2014.

Bibliography

Bibliography

[1] S.L. Glashow. Partial symmetries of weak interactions. *Nucl. Phys.*, 22:579–588, 1961. 1

[2] Steven Weinberg. A model of leptons. *Phys. Rev. Lett.*, 19:1264–1266, 1967. 1

[3] A. Salam and J.C. Ward. Electromagnetic and weak interactions. *Phys. Lett.*, 13(2):168 – 171, 1964. 1

[4] Richard P. Feynman. Very high-energy collisions of hadrons. *Phys. Rev. Lett.*, 23:1415–1417, 1969. 2

[5] Sidney D. Drell and Tung-Mow Yan. Massive lepton-pair production in hadron-hadron collisions at high energies. *Phys. Rev. Lett.*, 25:316–320, 1970. 5

[6] M. Chaichian, M. Hayashi, and K. Yamagishi. Angular distributions of high-mass dileptons in high-energy hadronic collisions. *Phys. Rev. D*, 25:130–142, Jan 1982. 5

[7] E. Mirkes and J. Ohnemus. W and Z polarization effects in hadronic collisions. *Phys. Rev. D*, 50:5692–5703, 1994. 5, 7

[8] V. M. Abazov et al. The Upgraded DØ Detector. *Nucl. Instr. and Meth. in Phys. Res. A*, 565:463, 2006. 12

[9] Torbjorn Sjostrand, Patrik Eden, Christer Friberg, Leif Lonnblad, Gabriela Miu, et al. High-energy physics event generation with PYTHIA 6.1. *Comput.Phys.Commun.*, 135:238–259, 2001. 20

[10] Sudeep Bhatia. talk. Talk given during EW meeting, June 2012. 32

[11] Sudeep Bhatia. talk. Talk given during EW meeting on June 26, 2012. 32